Theoretical and Applied Fracture Mechanics 117 (2022) 103187

Contents lists available at ScienceDirect

Theoretical and Applied Fracture Mechanics

journal homepage: www.elsevier.com/locate/tafmec

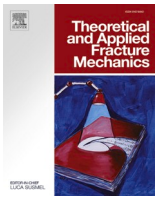

Crack propagation mechanism in rock-like specimens containing intermittent flaws under shear loading

Weibing Cai [a], Yong Li [b,c,*], Ke Gao [a,*], Kai Wang [d]

[a] Department of Earth and Space Sciences, Southern University of Science and Technology, Shenzhen 518055, Guangdong, China
[b] Geotechnical & Structural Engineering Research Center, Shandong University, Jinan 250061, Shandong, China
[c] School of Qilu Transportation, Shandong University, Jinan 250061, Shandong, China
[d] Shandong Expressway Co., Ltd, Jinan 250014, Shandong, China

ARTICLE INFO

Keywords:
Crack propagation
Shear behavior
Intermittent flaws
Stress field
Velocity field
Acoustic emission

ABSTRACT

The rock masses, especially with existing discontinuous joints, are prone to shear failure when subjected to constant changing stress in the direction perpendicular to the free face, which may result in tunnel collapse and slope slip instability in the processes of rock engineering construction. To better understand the effect of various joint geometries on the shear behavior of rocks, the mechanism of crack initiation, propagation, and coalescence in rock-like materials (a kind of cement mortar) with intermittent flaws under shear loading is investigated using both laboratory experiments and numerical simulations. The component of moment tensor is utilized to investigate the temporal and spatial evolution of acoustic emission events and determine the geometry state of the cracks. The major principal stress and velocity field are presented to distinguish crack types and study the stress evolution associated with crack propagation. The results reveal that for specimens with various flaw dip angles the propagation direction of all newly generated cracks is basically parallel to the shearing loading, and the failure patterns of specimens are mainly controlled by tensile fractures. When the flaw inclination angle reaches 45°, the evolution of the thickness of newly generated micro cracks is controlled by the type of stress field, and after peak strength its variation mainly occurs near the tips of the pre-existing flaws. The secondary cracks obtained from the velocity field analysis mainly include tensile, compressive-shear, tensile-shear and pure shear cracks rather than simple tensile cracks, and the secondary cracks appear instantly and abundantly on both sides of the specimen. The work may shed light on the mechanism of slope slip, and provide guidance to the safe construction of engineering projects.

1. Introduction

In the excavation processes of many rock engineering projects such as rock slopes, the rock masses adjacent to free faces are often suffered from shear loadings [1,2]. Especially, due to the existence of intermittent joints with different geometrical arrangements and scales, the shear behaviors of such rock masses are usually complicated. The discontinuous joints could not only reduce the strength of rock masses, but also induce new discontinuities [3]. Therefore, a profound understanding of the propagation and coalescence of intermittent joints under shear loading is crucial for predicting rock failure and optimizing rock engineering design.

Compared with the high–cost and time–consuming in-situ tests, laboratory experiment is an effective and efficient tool that has been widely used to qualitatively and quantitatively analyze the mechanical properties of engineering rock masses. Due to the ease of fabrication, a large number of laboratory experiments have been performed using rock-like materials to investigate the shear behaviors and properties of jointed rocks [4–7]. According to the direction and path of crack propagation, two types of cracks have been well summarized, i.e., the wing cracks and the secondary cracks. Generally, the wing cracks are typical tensile cracks initiated from the tips of a flaw along the direction of maximum principal stress. The secondary cracks are considered as shear cracks, which often occur instantly and abundantly when approaching the peak stress [8,9]. Henceforth, the term ‘flaw’ denotes artificially created (or pre-existing) crack or fracture, and the term ‘crack’ indicates

* Corresponding authors at: Geotechnical & Structural Engineering Research Center, Shandong University, Jinan 250061, Shandong, China (Y. Li). Department of Earth and Space Sciences, Southern University of Science and Technology, Shenzhen 518055, Guangdong, China (K. Gao).
E-mail addresses: yongli@sdu.edu.cn (Y. Li), gaok@sustech.edu.cn (K. Gao).

https://doi.org/10.1016/j.tafmec.2021.103187
Received 3 October 2021; Received in revised form 13 November 2021; Accepted 15 November 2021
Available online 18 November 2021

newly induced fracture by shear loading.

Previous studies mainly focus on the effect of flaw orientations [10], normal stiffness [11], joint surface roughness [12], initial opening [13] and normal loads [14] on the shear mechanism of single or parallel joint (s) in rock masses. These results reveal that the geometric configurations of pre-existing flaws determine the initiation of cracks, and the final failure patterns are controlled by the shear rates and normal loadings. In fact, compared with the coplanar joints, the existence of intermittent joints in nature makes the rock mechanical behavior more complicated, simply because of the intricate interaction between rock bridges and joints [15]. In this work, we perform a series of laboratory experiments to investigate the initiation and propagation of intermittent flaws in rock-like specimens under shear loading.

However, information such as the evolution of stress field, which controls the crack propagation and the process of microscopic characteristics during shear, cannot be readily and completely captured by laboratory experiments. Therefore, numerical simulation, owing to its rapidity and convenience, has been extensively employed to supplement the analysis of deformation and failure mechanism of jointed rocks [16–20]. The discrete element method (DEM), with great advantages in analyzing large deformation and rock failure, is very effective for studying crack coalescence process and complex interaction in discontinuous jointed rock masses [21–26]. Based on DEM, the mechanisms of asperity degradation of rock joints under shear loading was analyzed by Bahaaddini, et al. [27], and the results obtained from numerical simulation are in good agreement with physical experiments. Sarfarazi, et al. [28] adopted DEM to study the effect of various geometric configurations of joints on the failure mechanism of rock bridge. A series of other direct shear tests in rock masses have been simulated by employing the two-dimensional DEM-based particle flow code (PFC2D) [29–33]. Those simulation results demonstrate the capability of DEM for such applications in rock mechanics and practical rock engineering [34].

Most previous simulations mainly concentrate on the macroscopic mechanism of shear behavior in natural rock or rock-like material [35–37]. However, the mesoscopic mechanism on the evolution of stress and velocity fields induced by crack propagation and the complex interaction in jointed rocks under shear loading are rarely mentioned or investigated. In addition, the mechanism of energy evolution and source rupture of jointed rock under shear loading remains elusive. Fortunately, by introducing the moment tensor theory, the acoustic emission (AE) model has been developed in numerical simulations based on PFC2D [38], and provides a micro perspective to analyze the source rupture of rock masses. The simulation of AE events could not only enhance the understanding of failure mechanism of jointed rock masses, but also establish a solid foundation to investigate the injection-induced seismicity due to its capability of simulating micro seismicity. While recent work mainly focuses on the distribution of AE event magnitude and the effect of AE evolution on crack propagation [39–44], the relationships of crack propagation and the component of moment tensor are rarely mentioned. Therefore, further component analysis of moment tensor is necessary to facilitate the understanding of the source mechanism of rock shear failure.

In this paper, to obtain insights into the mesoscopic mechanism of crack coalescence in rock masses with intermittent joints, we first conduct a series of indoor direct shear tests on rock-like specimens containing intermittent pre-existing flaws with different geometrical arrangements. Since the through flaws is two-dimensional in essence, PFC2D is further adopted to give a thorough investigation of the shear behavior of jointed rocks. According to the relative motion between particles in PFC2D, we classify the velocity field into four types to distinguish the newly generated crack types in various loading stages. The average stress is also obtained from the simulation to analyze the evolution of stress magnitude and direction induced by crack propagation. Additionally, we decompose the moment tensors of AE events into three parts, i.e., the double couple (DC) part represents pure shear motion, the isotropy (ISO) part indicates isotropic volumetric change in the source (positive value represents tensile opening while negative represents compressive closure), and the compensated linear vector dipole (CLVD) part represents motion away or toward the source [45], and analyze the components of moment tensor to explore the temporal and spatial evolution of micro AE events and to determine the geometry state of cracks (crack opening or closing).

Table 1
Physico-mechanical parameters of cement mortar and sandstone.

Material	Compressive strength σ_c (MPa)	Tensile strength σ_t (MPa)	Young's modulus E (GPa)	Poisson's ratio ν	Density ρ (g/cm^3)
Cement mortar	58.25	5.62	11.63	0.20	2.38
Sandstone	20–170	4–25	3–35	0.02–0.25	2.10–2.40

The paper is organized as follows. In Section 2, we introduce the preparation of specimens (a kind of cement mortar) containing intermittent flaws with different geometrical arrangements and examine the effect of various flaw inclination angles on crack propagation and failure patterns. In Section 3, a mesoscopic parameters calibration is firstly performed prior to establishing the numerical models. Then, the acoustic emission simulations are conducted with various flaw inclination angles, and the stress and velocity filed obtained from PFC2D are analyzed to investigate the crack propagation and coalescence at various stress stages. It is worth noting that the experimental results in Section 2 also serve as the foundation for parameters calibration in Section 3, and likewise, the numerical simulations in Section 3 are the extension and supplement of the laboratory experiments. We conclude in Section 4

2. Experimental analysis

The laboratory experiments are used as a preliminary and qualitative investigation of the mechanism of crack coalescence in rock masses under shear. In this section, we first introduce the preparation process of the specimens and pre-existing flaws. The experiment steps and working principle of the shear test device are also presented. Then, the effects of various flaw inclination angles on crack propagation and failure patterns under shear loading are analyzed.

2.1. Specimen preparation

The cement mortar, as a common rock-like material, is selected for current laboratory shear tests. The material consists of Portland cement, quartz sand and water with a mass ratio of 1:2.34:1.35, respectively. A small amount of water reducing agent is mixed to ensure the maximum fluidity of specimens in the process of preparation. Table 1 presents the physico-mechanical parameters of cement mortar, which is close to that of natural rocks such as sandstone [46]. With a ratio between the tensile to compressive strength close to 1:10, the cement mortar is an ideal rock-like brittle material for studying the shear mechanism of jointed rock mass [23]. It should be noted that the rock-like material cannot completely capture the anisotropy and heterogeneities behaviors of actual rocks. However, through rock-like material, we can easily control the location and geometry of pre-existing flaws, and prepare similar specimens to quantitatively and qualitatively investigate the influences of specific factors on the mechanical behaviors of rocks.

The specimen dimensions are 150 mm × 150 mm × 70 mm (length × width × thickness). A plexiglass rectangular plate with slots is placed at the bottom of the mold, and the position and orientation of the slots are changing to form various combinations of flaw inclination angles. Pre-existing flaws are created by inserting two rectangular metal slices (1.0 mm in thickness and 20 mm in width) into the mortar paste at locations according to the slots on the plexiglass plate and removing them before the mortar begins to harden. After maintaining in the mold for 24 h, the specimens are removed from the mold and maintained in the

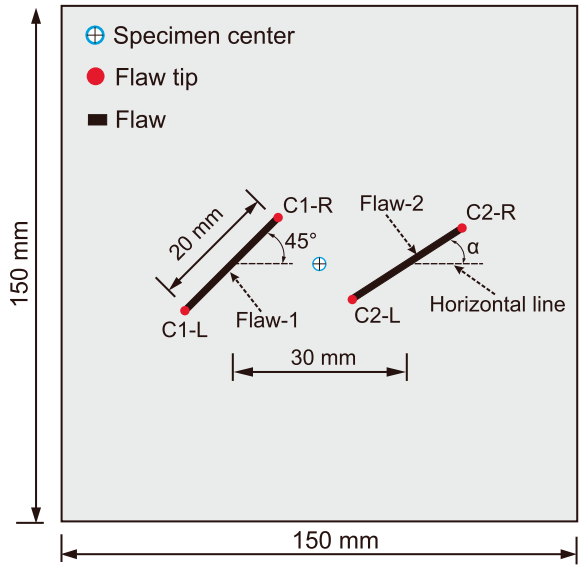

Fig. 1. Geometric configuration of intermittent flaws contained in the specimens. The pre-existing flaws are denoted as Flaw-1 and Flaw-2 from left to right, respectively. C1-L, C1-R, C2-L and C2-R represent the tips of flaws; α is the inclination angle of Flaw-2 (anticlockwise positive from right).

curing box with a temperature at 20 ± 2 °C and a humidity around 95% for seven days prior to the physical tests.

The two pre-existing flaws are placed in the middle of the specimen. Specifically, the centers of the two flaws are fixed with a distance of 30 mm; the line segment connecting the two flaw centers is parallel to the specimen boundary and the middle of the line segment coincides with the specimen center. The inclination angle of the left flaw (Flaw-1) is fixed at 45° (anticlockwise from right) in all specimens. By considering the cost of manufacturing and conducting the experiments, we vary the right flaw (Flaw-2) with six inclination angles (α) in the laboratory experiments, i.e., 30°, 45°, 60°, 120°, 135° and 150°. Based on the location of Flaw-2 tips relative to Flaw-1, these six angles can be classified into two groups, i.e., low inclination angles ($\alpha \leq 60°$) and high inclination angles ($\alpha \geq 120°$). It should be noted that the model size is large enough to avoid any boundary effect. The geometric configuration of the specimens is presented in Fig. 1.

2.2. Experimental steps

YUMT-1000 Microcomputer Control Electric Servo Rock Mechanics Universal Test System with servo motor drive technology and advanced sensor technology is used for current laboratory testing (see Fig. 2). The shear device is mainly composed of upper and lower shear boxes, in which the upper shear box moves from left to right under constant horizontal velocity and transfers shear loading to the upper part of specimen, while the lower shear box remains fixed. The roller plate is placed above the upper shear box to reduce the friction force induced by axial load, and then the metallic plate is placed between the axial loading device and roller plate so that the roller plate is subjected to a uniform force. The jack at the bottom provides an upward load to eliminate the effect of gravity of the specimen. The steel plates and hell blocks are designed to transfer uniform load to the specimen, and the existence of drum plate is to conveniently assemble the shear boxes. The shear rate is selected as 0.01 mm/s for all specimens, and the normal stress controlled by the servo hydraulic system is fixed at 2.0 MPa. The tangential shear stress is loaded after the normal compressive stress reaches the prescribed value. The shear stress and normal displacement are recorded by a data acquisition system during shear, and the whole crack generation process is filmed by a digital camera. The loadings are stopped when the residual shear stress reaches a stable value.

2.3. Experimental results

Because of the complex crack propagation procedure under shear loading, it is difficult to show the complete dynamic fracturing process. We only present in Fig. 3 the crack propagation procedure at two typical time stamps for each specimen. The model shearing direction is denoted by white arrows; the newly generated cracks are marked in red lines and numbered as Crack-n (n = 1,2…,) according to their emergence sequence.

Fig. 3a and b illustrate the crack propagation process with a Flaw-2 inclination angle of 30°. It can be observed that Crack-1 is initiated in the rock bridge region and ultimately connects C1-R and C2-L. Meanwhile, Crack–3 appears at C2-R as a typical shear crack and propagates towards the right edge of the specimen, while Crack–2 is initiated from the middle of Flaw-1 rather than the tips with a propagation direction opposite to that of Crack–3. The initiation and propagation of Crack-4 occur at the bottom edge of the specimen, which indicates that the crack is tensile based on the propagation path. As shear continues, Crack-5 is initiated at C1-L and propagates along the same direction as Crack-2 in a stable manner. Crack-6 is initiated near C2–R and propagates along the opposite direction of Crack-3. Crack-7 with a larger length appears in the upper right area of the specimen in a curvilinear path. For the model with Flaw-2 inclination angle of 45° (Fig. 3c-d), Crack-1 is initiated from C2-L and extends towards C1-R, and finally connects the pre-existing flaws and form a penetrating plane. At the same time, Cracks-2 and Crack-3 are initiated from C1-L and C2-R respectively and mainly propagate parallelly to the shear direction. Crack-4 initiates in the right area of the specimen at an arbitrary point. As shear continues, Crack-5 appears near C1-L and propagates toward

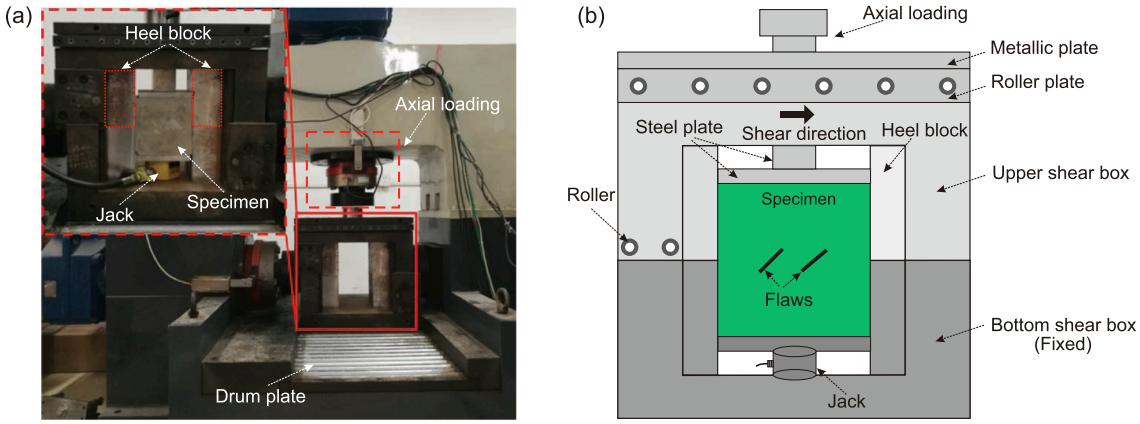

Fig. 2. Photograph of the shear testing device. (a) Physical photograph and (b) sketch chart.

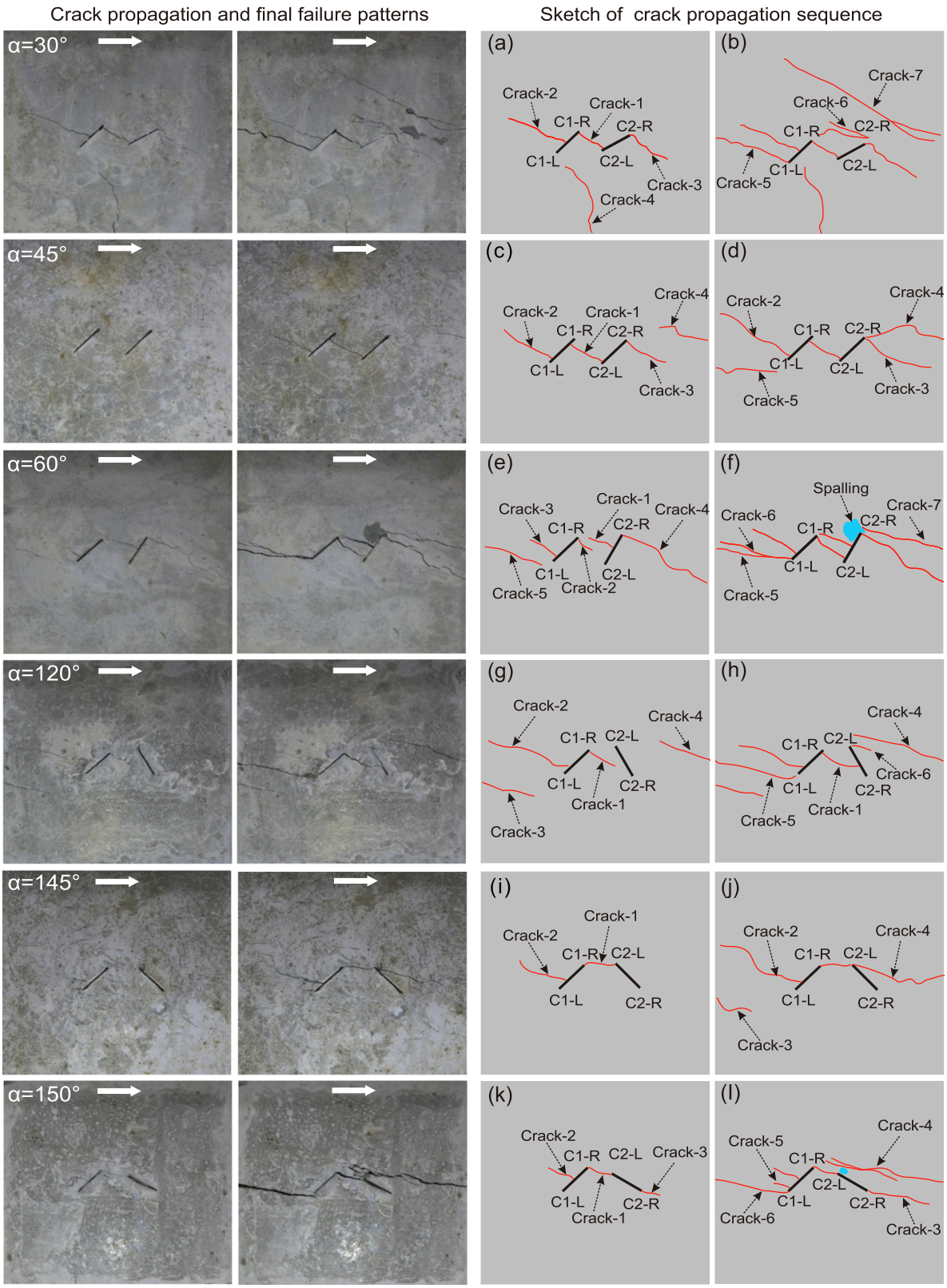

Fig. 3. Crack propagation process in specimens with different intermittent flaw combinations at two typical time stamps. The α denotes the inclination angle of Flaw-2. The two figures in the right column are sketches of crack propagation sequence corresponding to the two images in the left column, respectively. Cracks and model shear direction are denoted by red lines and white arrows, respectively. The blue patch represents the spalling area. (For interpretation of the references to color in this figure legend, the reader is referred to the web version of this article.)

the left side of the specimen. When the Flaw-2 inclination angle increases to 60° (Fig. 3e–f), Crack-1 and Crack-2 are initiated from the middle of Flaw-2 and C1-R, and propagate towards C1-R and C2–L, respectively; they both finally connect the pre-existing flaws. Crack-3 and Crack-5 both appear around C1-L, and propagate against the direction of shear, while Crack-4 is initiated from C2-R, and propagate towards the right side of the specimens. As shear continues, Crack-6 is also initiated from C1–L with the same propagation direction of Crack-5. A similar phenomenon occurs for Crack-7, while a spalling area is observed between Cracks-4 and Crack-7.

For the models with high Flaw-2 inclination angles such as $\alpha = 120°$ (Fig. 3g-h), Crack-1 occurs at C1-R and Crack-2 initiates near C1-L, and the propagation paths of both are basically parallel to the shear direction. Cracks-3 and Crack-4 appear in the left and right area of the specimen, respectively. As shear continues, Cracks-5 and Cracks-6 are initiated from C1-L and C2-L, respectively, and again propagate towards the maximum loading direction. The crack propagation for the model with $\alpha = 135°$ is shown in Fig. 3i-j. We first observe that Crack-1 appears in the rock bridge region and finally connects C1-R and C2-L, while Crack-2 is initiated near C1-L and propagates against the shear direction. Crack-2 continues to extend along the shear direction. Meanwhile, Crack-4 is initiated from C2-L and coalesces with Crack-1. In addition, Crack-3 appears in the left region of the specimen. For the model with $\alpha = 150°$ (Fig. 3k-l), it can be observed that Crack-1 appears in the bridge region and connects C1-R and C2-L. At the same time, Crack-2 is initiated at the middle portion of Flaw-1 and Crack-3 arises from C2-R. With the increasing shear displacement, Cracks–5 and Crack-6 are simultaneously initiated from C1-L and propagate towards the left of the specimen. Meanwhile, Crack-4 appears above Crack–3 with the same propagation path. A small spalling area can be clearly observed between Crack-4 and the tip (C2-L) of Flaw-2.

According to the above laboratory experiments, it is manifest that the propagation directions of all the newly generated cracks are basically parallel to the shear direction. A small number of cracks are initiated around the middle portion of Flaw-1 (e.g., specimens with $\alpha = 30°$ and 150°), rather than the tips of the flaws. The spalling region is prone to appear between parallel secondary cracks. Generally, far-field cracks without coalescing with the pre-existing flaws tend to extend in a stable manner with a propagation direction parallel to the new cracks. We also observe that when $\alpha = 30°$, 45°, 135° and 150° the cracks initiated from C1-R and C2-L are prone to form penetrating planes. Interestingly, when $\alpha = 60°$ and 120°, the new cracks initiated from C1-R prefer to propagate towards the middle of Flaw-2, indicating that the relative locations between Flaw-2 and C1-R determines the connection mode of the pre-existing flaws; this is likely due to the stress difference near the flaw tips. Additionally, for high inclination angles ($\alpha \geq 120°$), the newly generated cracks still are initiated from C2-L, which maybe is caused by the generation of penetrating plane between C1-R and C2-L. However, a profound understanding of crack generation induced by shear loading cannot be easily achieved without the assistance of numerical tools. Next, a series of numerical simulations based on PFC2D are further conducted to give a thorough and quantitative investigation regarding the mechanism of crack propagation and coalescence from microscopic viewpoint.

2.4. Numerical analysis

In this section, a mesoscopic parameter calibration is first performed based on the previous laboratory tests. The numerical models are then established to fully investigate the effect of Flaw-2 inclination angle on the temporal and spatial evolution of acoustic emission events. The stress filed, especially the magnitude and direction of maximum principal stress near the newly generated crack tips, is also analyzed. Finally, based on the trend of relative motion between particles, we classify the particle velocities into four types to distinguish the newly generated crack types during shear. Compared with the laboratory experiments, the specimens with Flaw-2 inclination angle of 75°, 90° and 105° are also considered in the numerical simulations, which is designed to comprehensively investigate the effect of Flaw-2 inclination angle on the initiation, propagation and coalescence of cracks.

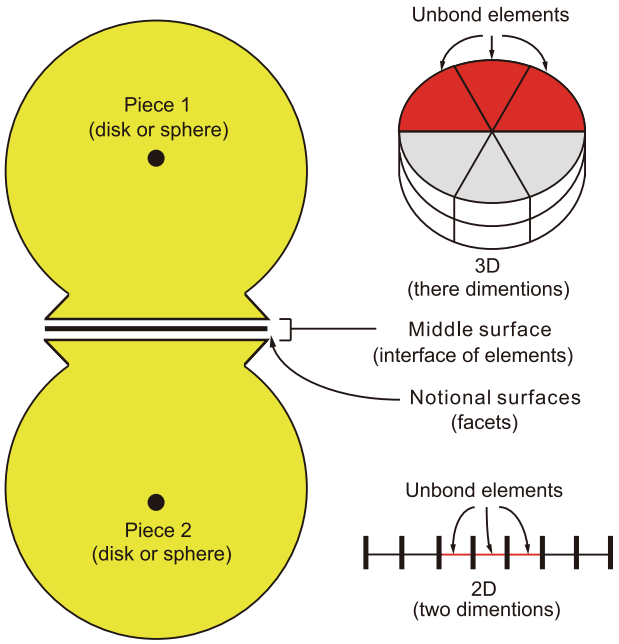

Fig. 4. Contact diagram of FJM.

Table 2
Microscopic parameters used in the numerical model.

Particle parameters	Values
Minimum radius R_{min} (mm)	0.4
Particle radius ratio R_{max}/R_{min}	1.66
Density ρ (g/cm^3)	1.18
Friction coefficient μ	0.3
Effective modulus E_c (GPa)	8.0
Normal/shear stiffness ratio k_n/k_s	2.0
Tensile strength $\bar{\sigma}_c$ (MPa)	21.5
Cohesion $\bar{c}$ (MPa)	18.5
Angle of internal friction $\bar{\phi}$ (°)	40.0
Bond effective modulus $\bar{E}_c$ (GPa)	5.5
Bond normal/shear stiffness ratio $\bar{k}_n/\bar{k}_s$	2.0
Radial elements N_r	1
Circumferential elements N_α	3

2.5. Numerical model calibration

The PFC2D, as a realization of DEM, is based on the Newton's second law and with great capability of numerically simulating the micro-mechanical behavior in brittle geo-materials. The flat-joint model (FJM) is adopted to simulate the mechanical properties of particle contacts, with its capability of eliminating the rotation of particles after bond breakage, which can effectively capture the mechanical behaviors of jointed rocks with high brittleness and internal friction angle [47,48]. The contact in FJM consists of a series of bonded or unbonded elements, and each bond breakage is denoted as a new micro crack. A typical FJM is demonstrated in Fig. 4, and a detailed explanation of it is presented in Appendix A.

In PFC2D, the mesoscopic parameters between particles directly determine the macroscopic mechanical properties of the specimens. Therefore, calibrating the mesoscopic parameters of FJM is the basis to

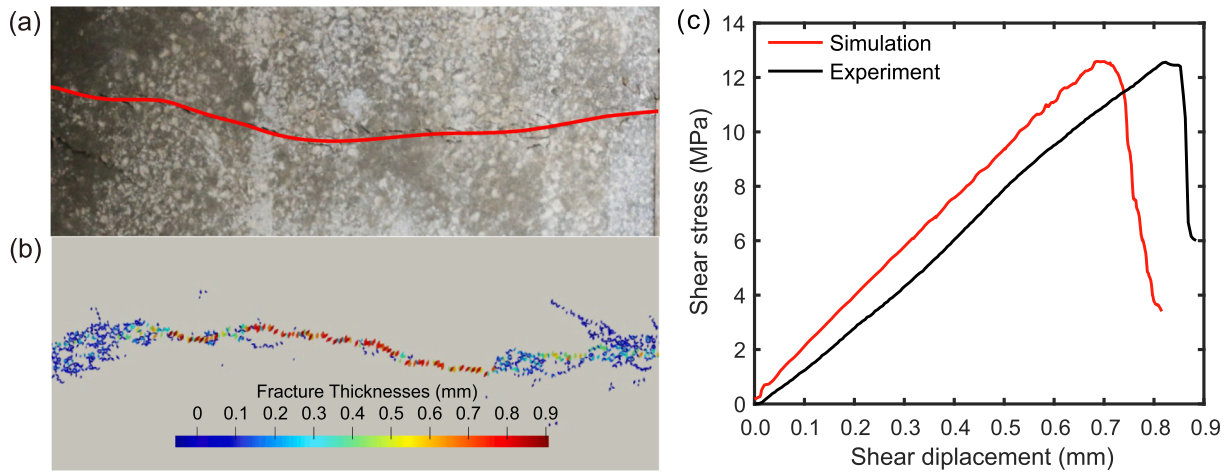

Fig. 5. Comparison between the laboratory experiment and the numerical simulation. (a) Experimental specimen failure. (b) Numerical specimen failure. (c) Curve of shear stress with shear displacement.

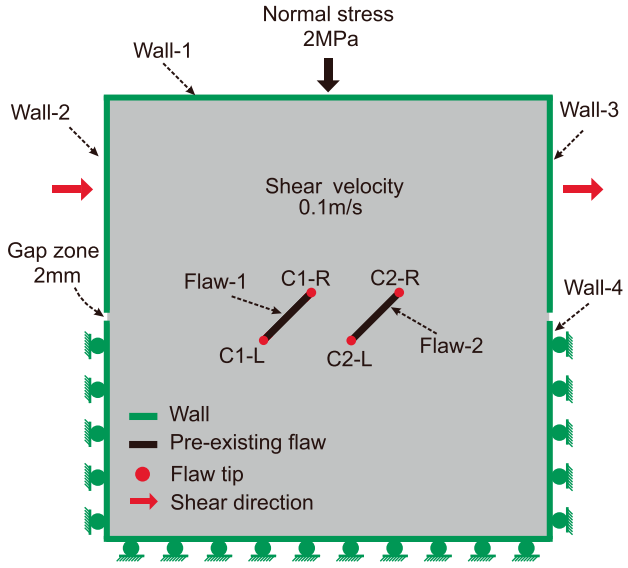

Fig. 6. Schematic representation of the numerical model.

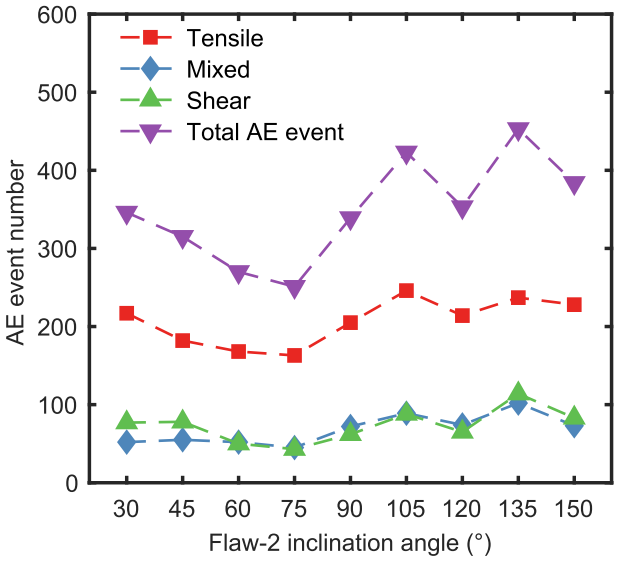

Fig. 7. Crack types and AE event number with various Flaw-2 inclination angles.

establish appropriate numerical models. To this end, a 'trial and error' method is adopted to guarantee the numerically simulated Young's modulus, Poisson's ratio, and shear strength are consistent with the laboratory shear tests on intact cement mortar specimens under a normal stress fixed at 2 MPa. The detailed calibration process can be found in our previous work [49], and the obtained appropriate mesoscopic parameters are tabulated in Table 2. Fig. 5 presents the comparison results in terms of failure pattern and the shear stress-shear displacement curve between the laboratory experiment and the numerical model utilizing the obtained mesoscopic parameters. The great consistency between the two demonstrates the accuracy of the numerical model. It should be noted that the shear displacement obtained from the laboratory experiment is slightly larger than that of the numerical simulation (~1.5 mm difference at peak shear stress point), which is due to the gradual closure of the micro cracks caused by specimen fabrication during initial loading [50].

2.6. Model setup

A schematic description of the numerical model is shown in Fig. 6. The loading rate is achieved by the movement of the 'walls' surrounding the model. The normal stress is applied vertically to the upper wall, and remains constant during the shearing process. The upper block is only allowed to move in the horizontal direction with a velocity of 0.1 m/s, while the lower block can move in the vertical direction. Although this loading velocity is much larger than the actual loading velocity in laboratory tests, the mechanical response of the system has not been changed when the model reaches a quasi-static equilibrium. The friction coefficient between the walls and the particles is set to zero to avoid the influence of the wall on the specimen. The shear force is obtained by tracking the reaction force on Wall-4 (Fig. 6).

2.7. AE characteristics

In this work, we view micro cracks occurred in close time and space spans as one single large AE event [51–53] and it thus could consist of several micro cracks, which further improves the accuracy of AE simulation [54]. Furthermore, based on the decomposition of moment tensor, each macroscopic crack can be divided into three types, i.e., tensile, mixed and shear cracks. Each macroscopic crack (AE event) contains one or multiple micro cracks triggered by a contact bond breakup. More details about the calculation of moment tensor and the introduction of

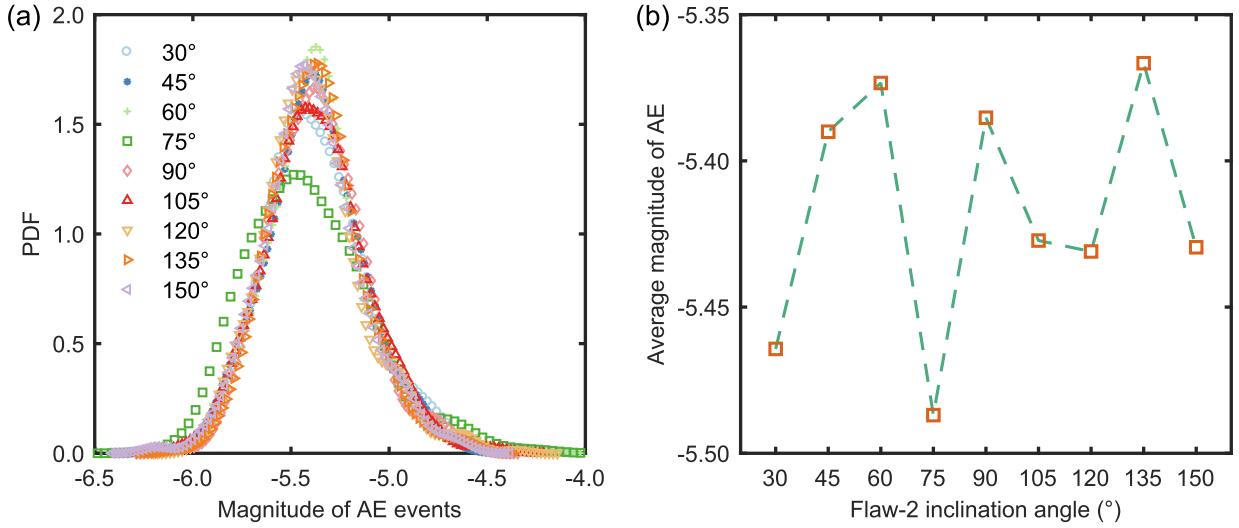

Fig. 8. AE events magnitude distribution. (a) PDFs of AE events magnitude for each specimen. (b) Average magnitude of AE events with Flaw-2 inclination angle. The black arrow marks the large distribution of AE events magnitude.

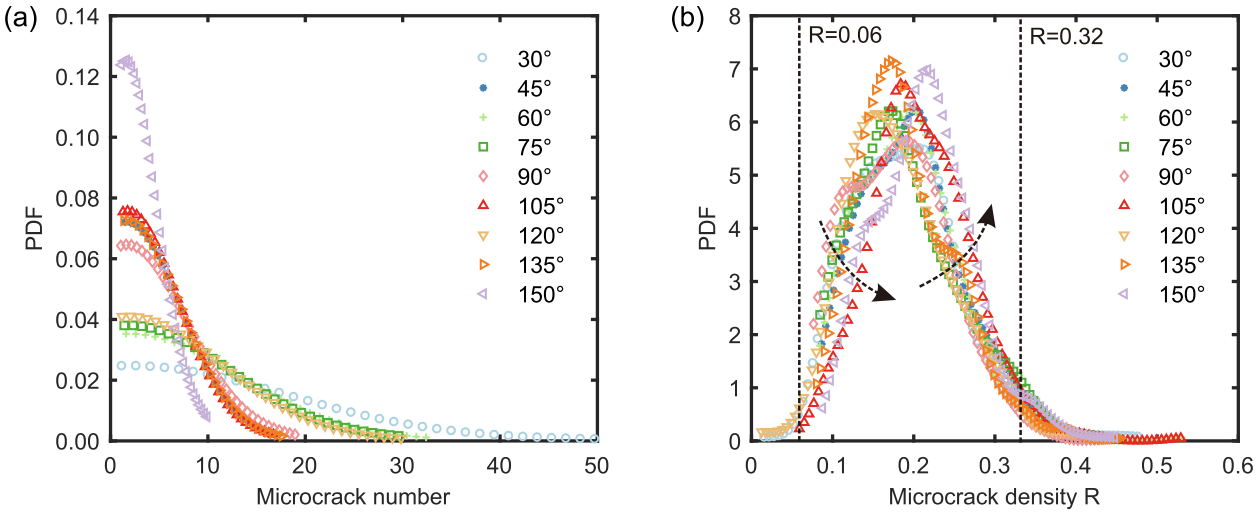

Fig. 9. Relationship between each AE event and the involved number of microcracks. (a) PDF of microcrack number per AE event. (b) PDF of microcrack density *R*. Black arrow with dashed line denotes the change trend of PDF of microcrack density with Flaw-2 inclination angle.

AE event in PFC2D can be found in Appendix B.

The influence of Flaw-2 inclination angle on the types of the generated cracks based on AE analysis is presented in Fig. 7. We can observe that in general the total number of AE events in specimens with high Flaw-2 inclination angles ($\alpha \geq 90°$) is larger than that in specimens with low Flaw-2 inclination angles ($\alpha \leq 75°$). This demonstrates that the opposite inclination direction setup for the two flaws (i.e., higher Flaw–2 inclination angles here, $\alpha \geq 90°$) could facilitate the generation of new fractures. For the specimens with low Flaw-2 inclination angles, the total number of AE events decreases with the increase of α; while the total number of AE events presents the opposite changing trend in specimens with high Flaw-2 inclination angles, although with fluctuations. This gives evidence that the closer the Flaw-2 to the horizontal direction (very low or very high α), the more new fractures will be generated. The number of tensile cracks is obviously larger than the mixed and shear cracks, which results in a similar changing trend of tensile cracks to that of the total AE events, and further reveals that the number of tensile cracks mainly dominates the spatial distribution of AE events. Interestingly, the numbers of mixed and shear cracks are basically around the same level, which implies that the variation of Flaw-2 inclination angle does not have much effect on the generation of mixed and shear cracks.

The statistical distribution of AE event magnitude for each specimen is presented in Fig. 8. As can be seen from Fig. 8a, the AE event magnitudes roughly follow a series of normal-like distributions concentrated in the range of −6.5 to −4.0 and peaked around −5.5. The similar distribution of AE event magnitudes has been observed in previous works [39,55,56], which further validates the accuracy of our models. It seems that the peak value of the probability distribution functions (PDFs) reaches the maximum for the specimen with $\alpha = 60°$ and the lowest when $\alpha = 75°$. We further plot the average magnitude of AE events for each specimen in Fig. 8b and can observe a fluctuation with respect the Flaw-2 inclination angle. Unfortunately, we cannot see a clear changing trend.

As mentioned earlier, each single AE event may consist of several micro cracks. We plot in Fig. 9 the distribution of microcrack number in single AE events for all the specimens. As can be seen from Fig. 9a, the PDF decreases roughly in a negative exponential manner, which means that most AE events only involve a small number of microcracks. For the specimen with $\alpha = 150°$, the maximum number of microcracks in a

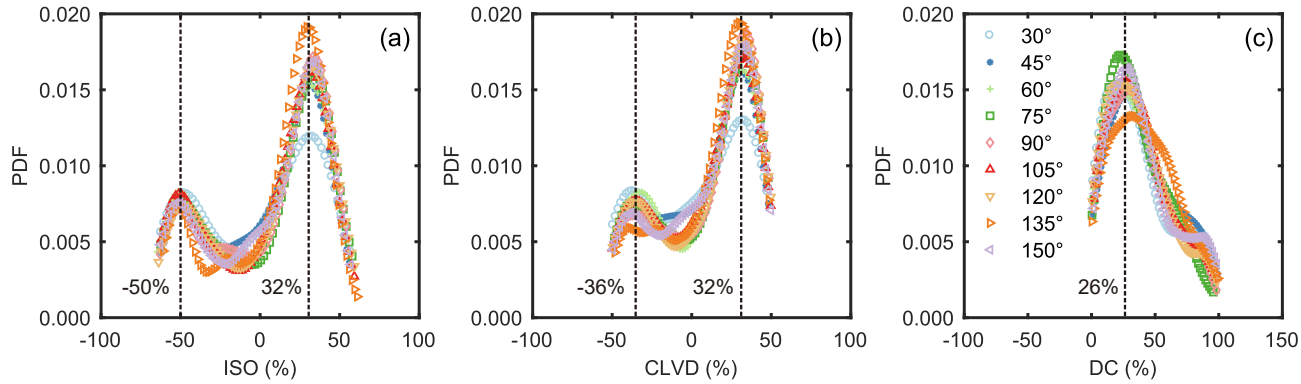

Fig. 10. PDFs of (a) ISO, (b) CLVD and (c) DC components of the moment tensor with different Flaw-2 inclination angles.

single AE event is mainly smaller than all the other specimens. While for the specimen with $\alpha = 30°$, the maximum number of microcracks in a single AE event can be as large as 50. This indicates that lower α has the capability to induce larger acoustic emissions, which means the specimens with similar inclination direction for both flaws could easily result in severe rock mass failure. Interestingly, the PDFs of microcrack number for $\alpha = 45°$, 135° and 60°, 120° are overlapping, which demonstrates that for the intermediate Flaw-2 inclination angles, the symmetrical geometric arrangement of pre-existing flaws has little influence on the variation of microcrack number in single AE events.

To further investigate the spatial characteristics of AE events and the corresponding microcracks, we define a variable $R = n/\pi r^2$ (n and r denotes the number of microcracks contained in a single AE event and its spatial spanning radius, respectively) as a microcrack density to describe the characteristics of microcracks in each AE event. Generally, a high crack density of AE implies a large damage extent of rock masses. The PDFs of microcrack density of single AE events for all specimens are presented in Fig. 9b. As can be observed, for both the largest ($R \geq 0.32$) and smallest R ($R \leq 0.06$), the PDFs present a similar changing trend, indicating that when a single AE event contains a very large or a very small number of microcracks, the distribution characteristics of microcracks in each AE event does not have much difference for all the specimens. For the specimens with relatively smaller R ($0.06 < R \leq 0.20$), the PDF decreases with the increase of α; while the opposite changing trend occurs for the specimens with relatively larger R ($0.20 < R < 0.32$). This reveals that when a single AE event contains intermediate microcracks ($0.06 < R < 0.32$), the spatial distribution of microcracks is greatly affected by the inclination angle of Flaw-2. Additionally, when $\alpha = 60°$, the distribution of R is wider than all other specimens, which is similar to the distributions of AE event magnitude in Fig. 8a, indicating that the higher the energy of an AE event, the larger the corresponding microcrack density would be.

We decompose the moment tensor of each AE event into three components, i.e., ISO, CLVD and DC. The PDFs of the three components for all specimens are presented in Fig. 10. It can be observed that the PDFs of ISO and CLVD are bimodal for all the specimens, while the PDFs of DC approximately obey a normal-like distribution. Compared with DC, the spatiotemporal evolution of Non-DC components (i.e., ISO and CLVD) are more complex. In Fig. 10a-b, the Non-DC components concentrates in the range of −55% to 55%, whereas the distribution of DC is within the range of 0 to 100% (Fig. 10c). For the positive Non-DC components, the peaks of PDF are heavily affected by the change of α, indicating that the crack opening is sensitive to the Flaw-2 inclination angle; both the PDFs of ISO and CLVD show a similar trend and reach the peaks at around 32%. For the negative Non-DC components, the PDFs of ISO and CLVD peak at −50% and −36%, respectively; these distributions are less affected by the variation of α. In addition, when $\alpha = 30°$, the peak of PDF in positive Non-DC components is obviously smaller than others. Overall, the PDFs of positive Non-DC components are generally wider than those of negative Non-DC components, which indicates that the number of opening cracks generated during shear is more than the closing cracks.

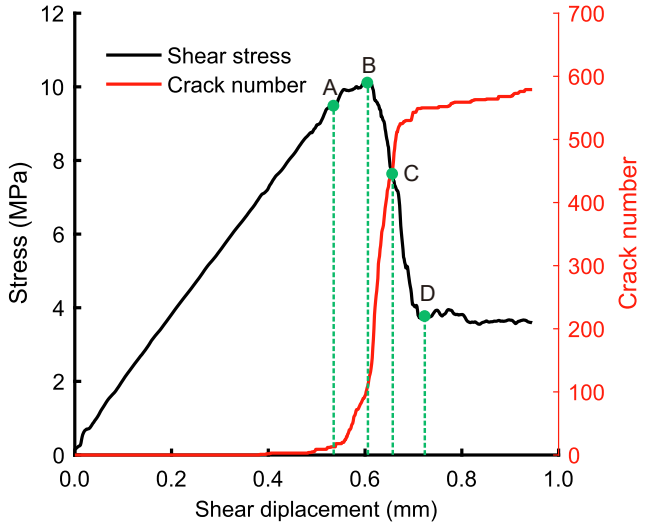

Fig. 11. Evolution of shear stress and crack number with respect to shear displacement for the specimen with $\alpha = 45°$. The corresponding stress values at point A, B, C, and D are 9.89 MPa, 10.15 MPa, 7.38 MPa and 3.72 MPa, respectively.

2.8. Evolution of stress field

To further study the detailed shear behavior of rock joints at various loading levels, the specimen with Flaw-2 inclination angle of 45° is taken as a representative example to investigate the mesoscopic mechanism of crack propagation and coalescence of intermittent flaws. Because stress and velocity field are constantly changing during shear loading, it is necessary to select several typical loading stages to examine the evolution of stress and velocity field associated with crack propagation. Fig. 11 shows the curve of shear stress and crack number with shear displacement for the specimen with Flaw-2 inclination angle of 45°. According to Fig. 11, the failure process of the specimen under shear loading can be divided into four phases, i.e., crack initiation phase (before point A), crack stable growth phase (from point A to B), the rapid growth phase (from point B to C) and the overall failure phase (from point C to D). Before the stress reaches point A, the specimens show good linear elastic characteristics, and the microcracks grow slowly until the axial stress is close to the peak strength. When specimens begin to enter the overall failure stage, the growth rate of microcracks increases approximately in an exponential manner with the shear displacement.

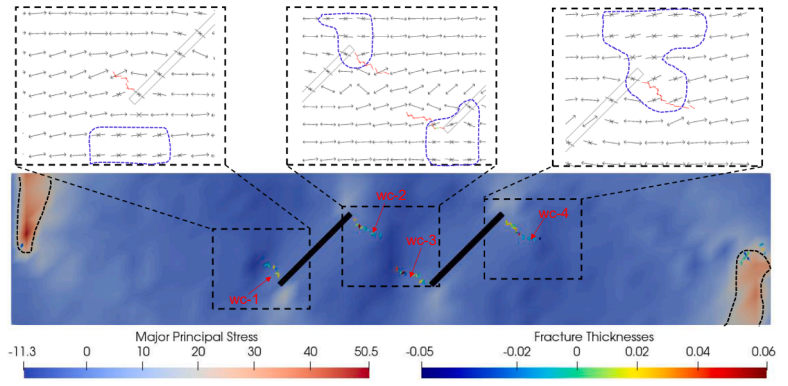

(a) Point A

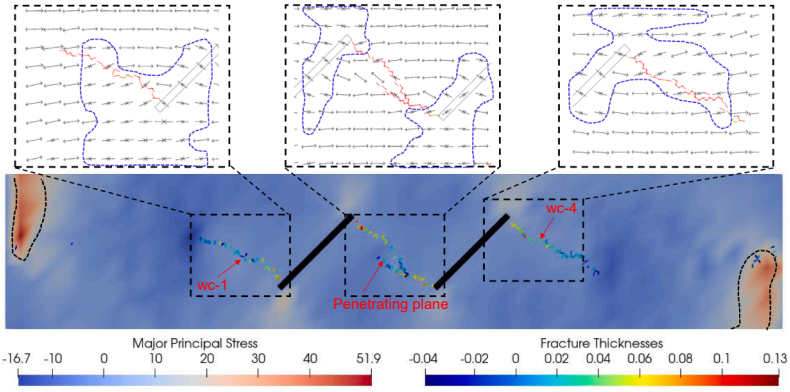

(b) Point B

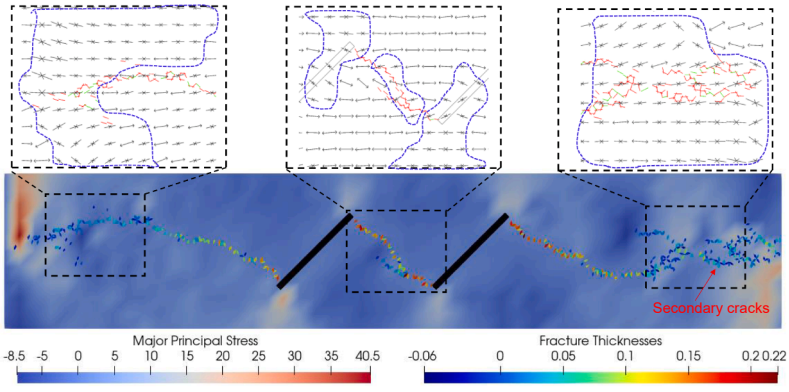

(c) Point C

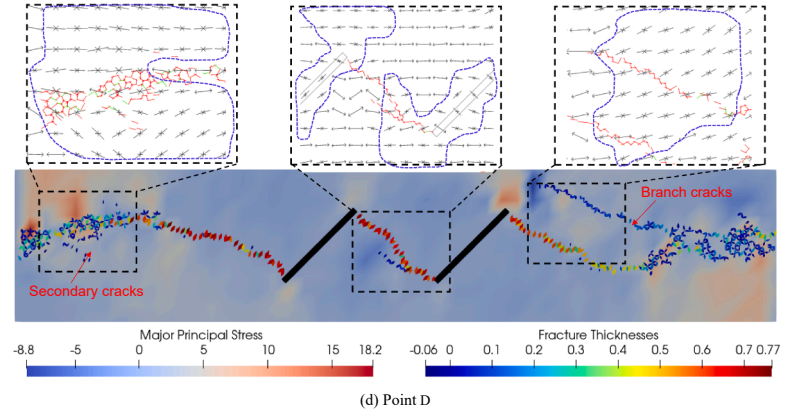

(d) Point D

Fig. 12. Snapshots of the major principal stress evolution at the four shearing stages (points A, B, C and D) mentioned in Fig. 11. The compressive stress is mainly distributed in the areas surrounded by the blue dashed lines. (For interpretation of the references to color in this figure legend, the reader is referred to the web version of this article.)

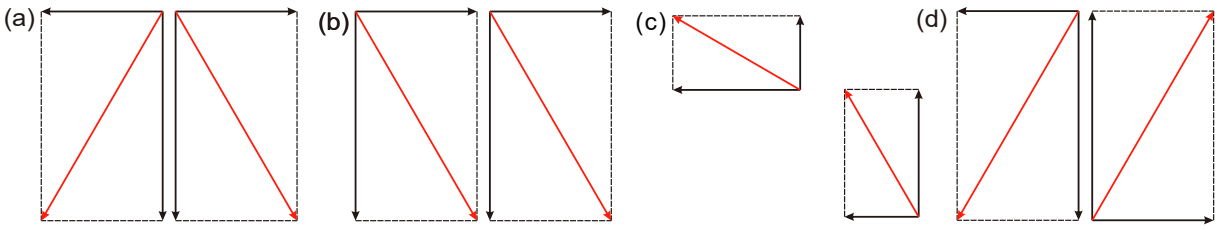

Fig. 13. A Schematic illustration of particle velocity field for the four types. (a) Type I; (b) Type II; (c) Type III; (d) Type IV.

We select the four turning points on the curve, i.e., points A, B, C, and D, corresponding to the shear stress of 9.89 MPa, 10.15 MPa, 7.38 MPa and 3.72 MPa, respectively, as the typical loading stages for further stress and velocity field analysis.

The stress field is crucial for analyzing the crack evolution mechanism in rock masses during the process of shear loading. However, unlike continuum mechanics based computational approaches such as finite element method (FEM), the stress field cannot be directly acquired in PFC2D. Therefore, the measurements are utilized to monitor and capture the average stress in a designated region of the specimen by Gauss integral of contact forces. More details of the calculation of stress tensor in a measurement can be found in Appendix C. During the shearing process, the stress field is visualized through importing data obtained from the measurements into an external post-processing software – ParaView, and the layout of all measurements covers the whole numerical model. The number of particles contained in each measurement is 15 to 20 with an overall radius of 1.5 mm, which fully consider the representativeness of specific points and the accuracy of the measured stress [57]. It should be pointed out that the location of pre-existing flaws is also set with measurements, which will slightly reduce the accuracy of the average stress around the pre–existing flaws. For convenience, only the evolution of major principal stress (magnitude and orientation) is analyzed in the following text. Additionally, since crack thickness can also reflect the shear behavior of rocks, we also calculate the micro crack thickness by subtracting the sum of the radius from the center of adjacent particles for all broken bonds at the four loading stages. However, it should be noted that the thickness calculated in such way in PFC2D may yield negative values when the particles overlap each other, i.e., subject to a compressive load.

The snapshots of the evolution of major principal stress at the four loading stages are shown in Fig. 12. The magnitude of the major principal stress is denoted in color following the geomechanics convention of compression positive. The insets above the stress distributions show the directions of major principal stress, and the areas under compressive stress are circled by blue dashed lines. Meanwhile, the tensile and shear microcracks in the stress vector image are represented by red and green lines respectively. For convenience, the wing cracks initiated at C1-L, C1-R, C2-L and C2-R are marked as wc-1, wc-2, wc-3 and wc-4, respectively.

It can be seen from Fig. 12a that when the shear stress reaches 8.98 MPa (point A), wc-1, wc-2, wc-3 and wc-4 begin to initiate at flaw tips, and except for wc–1, the length of the newly generated cracks are approximately 1/3 of the pre-existing flaw. Both tensile and compressive stress fields can be found around the pre-existing flaw tips, which implies that the initiation of wing crack involves both tensile and compressive stresses [50]. However, the tips of newly generated cracks are all tensile stress fields, indicating that the further crack propagation is fully controlled by tensile stress. It can be seen that the propagation direction of the crack is basically perpendicular to the direction of the tensile stress field near the crack tips, signaling that the wing crack will continue to propagate along the previous propagation direction. In addition, the maximum compressive stress is mainly concentrated around the shear surfaces on both sides of the specimen, and reaches 50 MPa approximately. When the shear stress peaks at 10.15 MPa (point B), the wing cracks wc–2 and wc-3 continue to propagate, and finally form a macroscopic penetrating plane, as shown in Fig. 12b; this is basically consistent with the experimental observations from Fig. 3c. Since the direction of the tensile stress field near the tip of wc-3 is roughly parallel to the fracture propagation direction, the length increment of wc-3 will be restrained. Meanwhile, the stress field on both sides of the penetrating surface is tensile, and the thickness of the crack near the flaw tips increases significantly. However, the propagation directions of wc-1 and wc-4 are not perpendicular to the direction of tensile stress field near wc-1 and wc-4 tips, indicating that the crack propagation direction would change. In addition, except for the slight increase of compressive stress field near the crack tip, the distribution of the whole stress field is mainly unchanged.

After the peak strength, the shear stress quickly drops to 7.38 MPa (point C). The wc-1 and wc-4 propagate to the left and right sides of the specimen and trigger a complete failure. As shown in Fig. 12c, branch cracks begin to initiate on the right side of the specimen. In the meantime, the compressive stress decreases to 40 MPa due to the stress relaxation during failure. Because the tensile and compressive stress field distributions in the secondary crack initiation area are extremely irregular, the propagation mechanism of secondary cracks is complicated. Additionally, the crack thickness near the flaw tips continue to increase, and the largest crack thickness is approximately 0.2 mm. The branch cracks continue to propagate due to the surrounding tensile stress field at the crack tips. As the shear displacement increases, the shear stress drops to 3.72 MPa (point D, Fig. 12d) and remains unchanged thereafter. A large number of secondary cracks appear on the left side of the specimen, and the branch cracks continue to propagate toward C2-R. Meanwhile, the crack thickness witnesses a significant increase, especially near the flaw tips. Although the tips are under tension, the stress field on both sides of the branch crack is compressive and thus yield a smaller crack thickness. Interestingly, the zones of compressive stress distribution become wider, although the system is accompanied with an apparent compressive stress drop.

Combined with the evolution analysis of the major principal stress magnitude and direction, it can be seen that the initiation of wing cracks is the result of the combined effect of tensile and compressive stress fields, which is different from previous studies [58,59]. Moreover, the propagation directions of wing cracks are determined by the geometric relationship between the directions of major principal stress and the existing cracks, which further explains the reason why the crack propagation direction observed in the experiments is basically parallel to the shear direction. The crack thickness is controlled by the type of the nearby stress field, and the wing crack thickness is larger than that of secondary and branch cracks. Furthermore, the distribution of secondary cracks is mainly surrounded by compressive stress fields, indicating that compressive stress controls the initiation and propagation of secondary cracks. During the shearing process, the maximum compressive stress is mainly distributed on both sides of the specimen. Although the maximum compressive stress continues to decrease after the peak strength, the distribution zones of compressive stress become more extensive.

3. Evolution of velocity field

In previous section, the proportions of shear, mixed and tensile crack

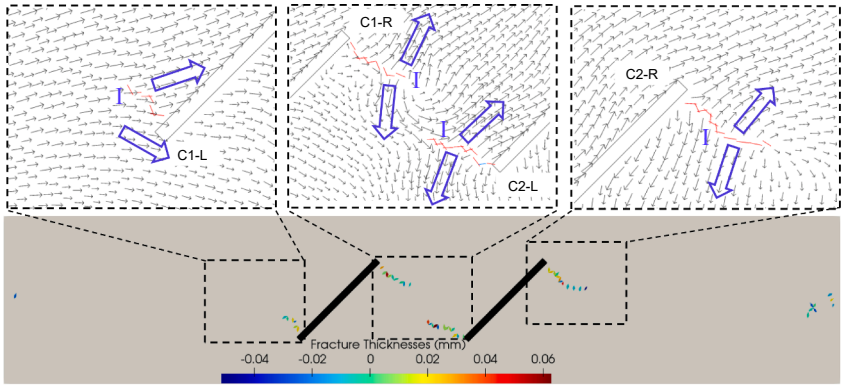

(a) Point A

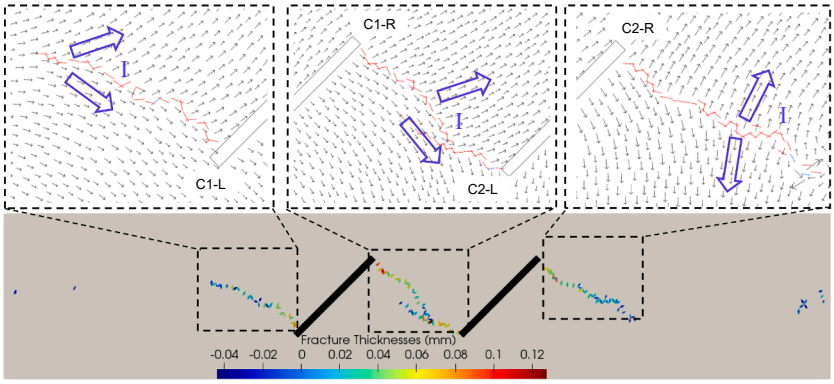

(b) Point B

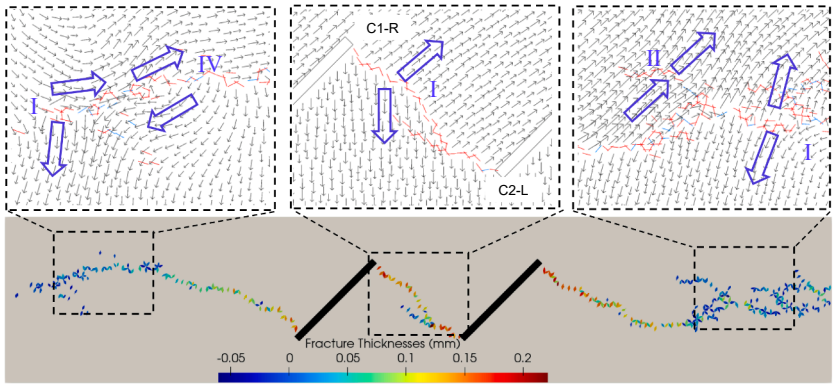

(c) Point C

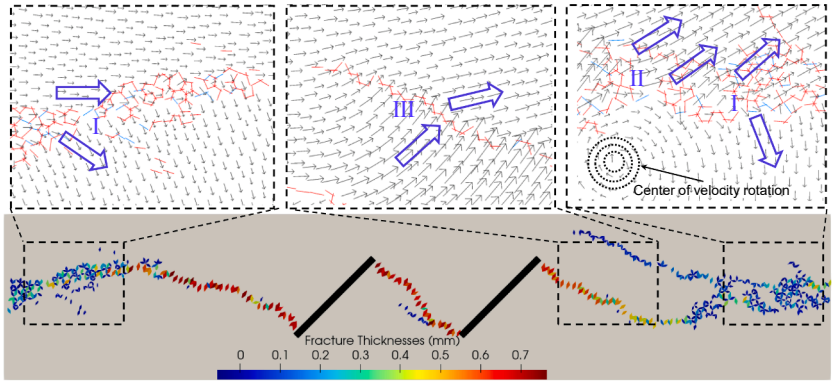

(d) Point D

Fig. 14. Snapshots of particle velocity in the four different loading stages (points A, B, C and D) mentioned in Fig. 11. The black lines with arrows represent the particle velocity, and the relative motion of particles near the newly generated cracks is denoted by thick blue arrows. (For interpretation of the references to color in this figure legend, the reader is referred to the web version of this article.)

types have been analyzed by decomposing the DC component of moment tensor (Fig. 7). Here, taking the same specimen with $\alpha = 45°$as an example, we further explore the type of newly generated cracks, determined by the direction of particle velocity on both sides of the crack, to give a profound understanding of the evolution of crack type under shear and validate the previous results. To this end, we divide the particle velocities into four types (i.e., Type I, II, III and IV) according to their directions. A schematic illustration of the four velocity types is shown in Fig. 13, and the details are described as follows.

(1) Type I: The horizontal components of the particle velocities on both sides of the newly generated crack are in opposite directions, while the vertical directions are the same. The relative motion of the particles is controlled by the horizontal component, and the newly generated crack is of tensile type.

(2) Type II: Both the horizontal and vertical components of the particle velocities are in the same direction and with similar magnitude, signaling that the newly generated crack is of compressive-shear type. While this type of particle velocity may inhibit further initiation and propagation of cracks.

(3) Type III: The horizontal and vertical components of the particle velocities are in the same direction but with different magnitudes, which gives a tensile-shear type newly generated crack.

(4) Type IV: Both the horizontal and vertical components of the particle velocities are in the opposite directions but with similar magnitude, which corresponds to the initiation of pure shear cracks.

The velocity of particles in the four loading stages (point A, B, C, and D in Fig. 11) are selected to analyze the evolution of velocity field and crack types, and the corresponding snapshots are shown in Fig. 14. The initiation and propagation of cracks lead to significant changes of particles velocity, and the relative motion between particles implies the physics of crack propagation and evolution. At point A, the wing cracks begin to initiate at flaw tips, and the particle velocity field on both sides of the newly generated cracks near the flaw tips are all Type I, which indicates a series of tensile cracks and is consistent with the analysis in Fig. 12a. At point B, the wing cracks at C1-R and C2-L continue to propagate and reach each other. However, the particle velocity fields on both sides of the newly generated cracks are still type I, and it shows that all the newly generated cracks prior to the peak strength are of tensile types.

With the increase of shear displacement until point C, the cracks propagate to the left and right boundaries of the specimen, and finally form a macroscopic penetrating plane. In addition, secondary cracks begin to accumulate on the right side of the specimen. The particle velocity field between the pre-existing flaws remains unchanged, while on both sides of the specimen it becomes extremely complicated. The particle velocity field on the left side of the specimen is mainly Type I and IV, so both shear and tensile cracks are initiated together. The particle velocity field on both sides of the branch cracks on the right side of the specimen is type II, indicating that the newly generated cracks are of compressive-shear type. At point D, a large number of secondary cracks appear on both sides of the specimen. The particle velocity field on the left side of the specimen becomes Type I, indicating a series of tensile cracks. Nevertheless, the velocity field on the right side of the specimen have not changed significantly. Additionally, the velocity field on both sides of the branch crack becomes Type III, suggesting that the newly generated cracks near branch cracks are of tensile-shear type. Interestingly, we can observe a clear particle rotation near the secondary cracks (see black circles in Fig. 14d), which signifies the complex mechanics of secondary crack initiation and propagation from the perspective of vortex evolution [60].

The above analysis demonstrates that before the peak strength, only a small number of tensile cracks are initiated, and shear cracks mainly appear after failure. The secondary cracks are extremely complex, which may include four types such as tensile, compressive-shear, tensile-shear and pure shear. The Type II, III and IV IV particle velocity field induced by the initiation and propagation of secondary cracks are related to the shear stress field. The branch cracks only appear on the right side of the specimen, and their types vary from compressive-shear to tensile-shear due to the relaxation of compressive stress after the peak strength.

4. Conclusions

In this study, the initiation and propagation of cracks in rock containing intermittent flaws under shear loading is investigated using both laboratory experiments and numerical simulations. In the laboratory experiments using rock-like specimens, the propagation direction of all newly generated cracks is basically parallel to the shear direction, which is consistent with the previous studies [11,61]. However, different from the uniaxial compression test with pre-existing flaws, a small number of cracks are initiated from the middle portion, rather than the tips of the pre-existing flaw. This indicates that the relative location of crack tips determines the connection mode of pre-existing flaws, which is likely due to the stress difference near the crack tips. Spalling region is prone to appear between two parallel new cracks, which is due to the intersection of newly generated crack networks.

The number of tensile cracks is obviously more than that of mixed and shear cracks, indicating that the failure pattern of specimens is mainly controlled by tensile failure during the shear process. The numbers of mixed and shear cracks are basically around the same level, which reveals that the variation of flaw inclination angle does not have much effect on the distribution of mixed and shear cracks. When the Flaw-2 inclination angle $\alpha = 150°$, the number of microcrack in each AE event is smaller than all other specimens; while when $\alpha = 30°$, the number of microcracks in each AE event reaches maximum, indicating the smaller α induces high energy acoustic emission events, which may provide guidance to eliminate instability of rock masses in the excavation processes of tunnels and slopes. Interestingly, the PDFs of the magnitude of AE events and the components of DC basically obey normal-like distributions. However, the pre-existing flaws only can affect the local distribution of AE event magnitudes rather than the whole specimen. Furthermore, the distribution of Non-DC (ISO and CLVD) components with positive values is wider than that with negative values, which suggests that the number of open cracks is more than that of the closed cracks [62]. Therefore, the analysis of Non-DC components may enhance the understanding of the geometric state (opening or closing) of fracture networks.

For the stress field analysis, we have found that the relationship between the directions of major principal stress and existing crack propagation determine the further crack propagation direction, and the crack thickness evolution is controlled by the type of stress field near the newly generated cracks and the velocity direction of the particle. Additionally, the maximum compressive stress is mainly distributed on both sides of the specimen, and the distribution zones are slightly increased after the peak strength due to the stress relaxation. Tensile cracks are primarily initiated at flaw tips prior to the peak strength; while secondary cracks appear abundantly on both sides of the specimen due to the rapid decrease of the shear stress, which is consistent with the uniaxial compression test with pre-existing flaws in rock-like specimens [19,63–65]. Moreover, the types II, III and IV velocity field for particles induced by the initiation and propagation of secondary cracks are related to the shear stress field. Interestingly, the center of particle rotation (see black circles in Fig. 14d) appears near the secondary cracks rather than the specimen center, which may be caused by the shear direction and the anisotropy of the specimens. Furthermore, the occurrence of particle rotation center is associated with the evolution of secondary cracks, and this phenomenon of particle rotation has been utilized to investigate the evolution of shear bond from the perspective of vortex [60], which may provide an innovative method to elucidate the complex mechanism of secondary crack initiation and propagation.

However, the distance and length of pre-existing flaws may also have impact on the failure mechanism of rock masses. In the future work, we will pay attention to the effect of various spatial location and length of

flaws on crack initiation and propagation. Additionally, the normal stress is fixed at 2 MPa in the current analysis, while the impact of different normal stress on the temporal and spatial evolution of acoustic emission events may worth a future investigation as well. Nevertheless, the work may help understand the fundamental mechanism of slope slip, and provide guidance to the safe construction of rock engineering projects.

Declaration of Competing Interest

The authors declare that they have no known competing financial interests or personal relationships that could have appeared to influence the work reported in this paper.

Acknowledgments

This research was funded by the National Natural Science Foundation of China (Grant No. 51879149), Taishan Scholars Project Foundation of Shandong Province, and the Free Exploration Foundation of School of Qilu Transportation, Shandong University, P. R. China (Grant No. 2019B47_1).

Appendix A:. Constitutive relation of contact in FJM (flat-joint model)

In FJM, the contact involves several elements subjected to external forces. Partial elements will be destroyed when the loading reaches strength limitation, while the remaining elements will keep resistance. Therefore, the FJM can simulate the damage of rock materials. For the unbonded part, the shear strength follows the Coulomb slip criterion:

$$\tau_r = \begin{cases} -\overline{\sigma} tan\phi_r & \overline{\sigma} < 0 \\ 0 & \overline{\sigma} = 0 \end{cases}$$

where ϕ_r is the residual friction angle and $\overline{\sigma}$ is the normal stress of an element. The shear stress will remain unchanged when it satisfies the relationship $\tau_{max}^{(e)} \leqslant \tau_r$; otherwise, the sliding criterion will be implemented if the relationship becomes $\tau_{max}^{(e)} = \tau_r$.

For the bonded part, the shear strength follows the Mohr-Coulomb criterion:

$$\tau_c = c_b - \overline{\sigma} tan\phi_b$$

where ϕ_b is the internal friction angle, c_b is the cohesion. When the shear stress of the element satisfies the relationship $\tau_{max}^{(e)} \leqslant \tau_b$, the stress will remain unchanged; otherwise, the state of element will change from bond to non-bond when the element suffers from breakup, and then the residual friction between particles begin to support loading. Thus, the FJM has great advantage to simulate crack propagation of brittle materials.

Appendix B:. Micro acoustic emission (AE) simulation

When contact bond between particles breakup occurs, the relative motion of particles on both sides of the contact will change, which further leads to the change of the contact force around source particles (see Fig. B1). Hence, the moment tensor can be obtained by capturing the change of contact force, i.e.,

$$M_{ij} = \sum_s \Delta F_i R_j \tag{B.1}$$

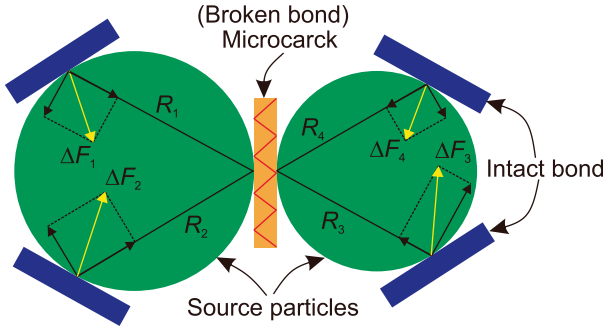

Fig. B1. A schematic diagram of the moment tensors.

where ΔF_i and R_j are the component of contact force change and the distance measured from contact to AE event center, respectively. In PFC, ΔF_i can be obtained by subtracting the contact force at the initial rupture from the current contact force during the duration of an AE event. In this work it is assumed that the location of microcrack is the geometric center of an AE event when it contains only one microcrack. If more than one bond breakage makes up the single event, then the geometrical center of the event is obtained by averaging the location of microcracks. To determine the duration of AE events, we assume that the source wave of each AE event is a shear wave, and the initiation and propagation speed of the microcrack is half of the shear wave speed in rocks. If the time required from the moment of microcrack generation to the time when the shear wave induced by microcrack transmitted to the boundary of the area is denoted as T_s, the duration of AE events can be marked as 2 T_s. For the duration of each AE event, we have

$$T_s = \frac{R_{aver}}{V_s} \tag{2}$$

where R_{aver} denotes the average radius of source particles, and V_s is the shear wave velocity of rock at 2000 m/s in this work.

It is not feasible to calculate the magnitude of an AE event by moment tensor at any time during its duration due to high computing costs. To improve the computational efficiency, only the maximum scalar moment M_0 generated within the duration is recorded in this study, which can be obtained by

$$M_0 = \sqrt{0.5 \times \sum_{j=1}^{3} m_j^2} \tag{B.3}$$

where m_j is the eigenvalue of the moment tensor matrix. According to the scalar moment, the magnitude M_W of an AE event can be further calculated by

$$M_W = \frac{2}{3} log M_0 - 6 \tag{B.4}$$

Since the moment tensor in DEM is a symmetric tensor and the three eigenvalues are all real numbers, the moment tensor can be decomposed as [66]

$$\begin{aligned} \boldsymbol{M} &= \begin{bmatrix} M_1 & 0 & 0 \\ 0 & M_2 & 0 \\ 0 & 0 & M_3 \end{bmatrix} = \frac{1}{3}(M_1 + M_2 + M_3)\begin{bmatrix} 1 & 0 & 0 \\ 0 & 1 & 0 \\ 0 & 0 & 1 \end{bmatrix} \\ &+ \frac{1}{2}(M_1 - M_3)\begin{bmatrix} 1 & 0 & 0 \\ 0 & 1 & 0 \\ 0 & 0 & -1 \end{bmatrix} + \frac{1}{6}(2M_2 - M_3 - M_1)\begin{bmatrix} -1 & 0 & 0 \\ 0 & 2 & 0 \\ 0 & 0 & -1 \end{bmatrix} \\ &= \boldsymbol{M}^{\mathrm{ISO}} + \boldsymbol{M}^{\mathrm{DC}} + \boldsymbol{M}^{\mathrm{CLVD}} \end{aligned} \tag{B.5}$$

where $\boldsymbol{M}^{\mathrm{ISO}}$ is the isotropic part of the moment tensor, $\boldsymbol{M}^{\mathrm{DC}}$ is the moment tensor for pure shear cracks, $\boldsymbol{M}^{\mathrm{CLVD}}$ is the compensated linear dipole, and M_1, M_2 and M_3 are the three eigenvalues of the moment tensor. For an AE event, the proportion of these three components are denoted as ISO, CLVD and DC, which can be calculated using

$$ISO = \frac{M_1 + M_2 + M_3}{|M_1 + M_2 + M_3| + M_1 - M_3} \tag{B.6}$$

$$CLVD = \frac{M_1 + M_3 - 2M_2}{|M_1 + M_2 + M_3| + M_1 - M_3} \tag{B.7}$$

and

$$DC = \frac{M_1 - M_3 - |M_1 + M_3 - 2M_2|}{|M_1 + M_2 + M_3| + M_1 - M_3} \tag{B.8}$$

respectively, and the scale factors ISO, CLVD and DC satisfy

$$|ISO| + |CLVD| + DC = 1 \tag{B.9}$$

Based on the DC component, an AE event can be further classified as a tensile source if $0 \leq \mathrm{DC} < 40\%$, a mixed source if $40\% \leq \mathrm{DC} \leq 60\%$, and a shear source if $60\% < \mathrm{DC} \leq 100\%$. Therefore, we can conveniently distinguish the types of cracks in the process of shear loading by calculating the proportion of DC.

Appendix C:. Calculation of stress tensor in a measurement

In PFC2D, contact forces and particles displacements are discrete, while stress is a continuum quantity. Therefore, to study the material behavior on a microscale by stress, the averaging stress is adopted from the microscale to a continuum. The average stress $\overline{\boldsymbol{\sigma}}$ in a measurement region of volume V can be computed by

$$\overline{\sigma} = -\frac{1}{V}\sum_{N_c} F^{(c)} \otimes L^{(c)} \tag{C.1}$$

where N_c is the number of contacts that lie in the measurement region or on its boundary, $\boldsymbol{F}^{(c)}$ is the contact force vector, $\boldsymbol{L}^{(c)}$ is the branch vector joining the centroids of the two bodies in contact, and $\otimes$ denotes outer product. For convenience, we only analyze the evolution of major principal stress σ_1 for each measurement, i.e.,

$$\sigma_1 = \frac{\sigma_x + \sigma_y}{2} + \sqrt{\left(\frac{\sigma_x - \sigma_y}{2}\right)^2 + \tau_{xy}^2} \tag{C.2}$$

where σ_x, σ_y and τ_{xy} is the component of the stress tensor $\overline{\sigma}$, respectively.

References

[1] D. Cen, D.a. Huang, Y. Song, Q. Jiang, Direct Tensile Behavior of Limestone and Sandstone with Bedding Planes at Different Strain Rates, Rock Mech. Rock Eng. 53 (6) (2020) 2643–2651.

[2] D.a. Huang, D. Cen, Y. Song, Comparative Investigation on the Compression-Shear and Tension-Shear Behaviour of Sandstone at Different Shearing Rates, Rock Mech. Rock Eng. 53 (7) (2020) 3111–3131.

[3] A. Bobet, H.H. Einstein, Fracture coalescence in rock-type materials under uniaxial and biaxial compression, Int. J. Rock Mech. Min. Sci. 35 (7) (1998) 863–888.

[4] S. Fereshtenejad, J.-J. Song, Applicability of Powder-based 3D Printing Technology in Shear Behavior Analysis of Rock Mass Containing Non-persistent Joints, J. Struct. Geol. 143 (2020), 104251.

[5] C. Gehle, H.K. Kutter, Breakage and shear behaviour of intermittent rock joints, Int. J. Rock Mech. Min. Sci. 40 (5) (2003) 687–700.

[6] M. Kleepmek, S. Khamrat, T. Thongprapha, K. Fuenkajorn, Displacement velocity effects on rock fracture shear strengths, J. Struct. Geol. 90 (2016) 48–60.

[7] K.e. Zhang, P. Cao, J. Meng, K. Li, W. Fan, Modeling the Progressive Failure of Jointed Rock Slope Using Fracture Mechanics and the Strength Reduction Method, Rock Mech. Rock Eng. 48 (2) (2015) 771–785.

[8] L.N.Y. Wong, H.H. Einstein, Systematic evaluation of cracking behavior in specimens containing single flaws under uniaxial compression, Int. J. Rock Mech. Min. Sci. 46 (2) (2009) 239–249.

[9] C.H. Park, A. Bobet, Crack coalescence in specimens with open and closed flaws: A comparison, Int. J. Rock Mech. Min. Sci. 46 (5) (2009) 819–829.

[10] A. Ghazvinian, V. Sarfarazi, W. Schubert, M. Blumel, A Study of the Failure Mechanism of Planar Non-Persistent Open Joints Using PFC2D, Rock Mech. Rock Eng. 45 (2012) 677–693.

[11] Y. Zhang, Y. Jiang, D. Asahina, Z. Wang, Shear behavior and acoustic emission characteristics of en-echelon joints under constant normal stiffness conditions, Theor. Appl. Fract. Mech. 109 (2020), 102772.

[12] M. Asadizadeh, M. Moosavi, M.F. Hossaini, H. Masoumi, Shear Strength and Cracking Process of Non-persistent Jointed Rocks: An Extensive Experimental Investigation, Rock Mech. Rock Eng. 51 (2) (2018) 415–428.

[13] Y. Li, J. Oh, R. Mitra, B. Hebblewhite, Experimental Studies on the Mechanical Behaviour of Rock Joints with Various Openings, Rock Mech. Rock Eng. 49 (3) (2016) 837–853.

[14] V. Sarfarazi, H. Haeri, Effect of number and configuration of bridges on shear properties of sliding surface, J. Min. Sci. 52 (2) (2016) 245–257.

[15] X.-P. Zhang, Q. Liu, S. Wu, X. Tang, Crack coalescence between two non-parallel flaws in rock-like material under uniaxial compression, Eng. Geol. 199 (2015) 74–90.

[16] S. Jiang, Y. Ye, X.u. Li, S. Liu, J. Liu, D. Yang, Y. Tan, DEM modeling of crack coalescence between two parallel flaws in SiC ceramics, Ceram. Int. 45 (12) (2019) 14997–15014.

[17] A. Abdollahipour, M. Fatehi Marji, A. Yarahmadi Bafghi, J. Gholamnejad, DEM simulation of confining pressure effects on crack opening displacement in hydraulic fracturing, Int. J. Min. Sci. Technol. 26 (4) (2016) 557–561.

[18] M.P.J. Schöpfer, S. Abe, C. Childs, J.J. Walsh, The impact of porosity and crack density on the elasticity, strength and friction of cohesive granular materials: Insights from DEM modelling, Int. J. Rock Mech. Min. Sci. 46 (2) (2009) 250–261.

[19] X.-P. Zhang, P.-Q. Ji, J. Peng, S.-C. Wu, Q. Zhang, A grain-based model considering pre-existing cracks for modelling mechanical properties of crystalline rock, Comput. Geotech. 127 (2020), 103776.

[20] M. Wu, R. Huang, J. Wang, DEM simulations of cemented sands with a statistical representation of micro-bond parameters, Powder Technol. 379 (2021) 96–107.

[21] S. Vahab, H. Hadi, F. Mohammad, Fracture Mechanism of Brazilian Discs with Multiple Parallel Notches Using PFC2D, Period. Polytech. Civ. Eng. 61 (2017).

[22] M.M. Kou, Y.J. Lian, Y.T. Wang, Numerical investigations on crack propagation and crack branching in brittle solids under dynamic loading using bond-particle model, Eng. Fract. Mech. 212 (2019) 41–56.

[23] B. Li, S. Yu, W. Zhu, W. Cai, L. Yang, Y. Xue, Y. Li, The Microscopic Mechanism of Crack Evolution in Brittle Material Containing 3-D Embedded Flaw, Rock Mech. Rock Eng. 53 (11) (2020) 5239–5255.

[24] C. Wei, Y. Li, W. Zhu, S. Li, S. Wang, H. Wang, Experimental observation and numerical investigation on propagation and coalescence process of multiple flaws in rock-like materials subjected to hydraulic pressure and far-field stress, Theor. Appl. Fract. Mech. 108 (2020), 102603.

[25] H. Xu, Y. Qin, G. Wang, C. Fan, M. Wu, R. Wang, Discrete element study on mesomechanical behavior of crack propagation in coal samples with two prefabricated fissures under biaxial compression, Powder Technol. 375 (2020) 42–59.

[26] B.-X. Li, S. Yu, W.-S. Zhu, L. Yang, W.-B. Cai, Y.-G. Xue, Y. Li, The crack coalescence mode and physical field evolutionary characteristics of a brittle material containing two 3-D parallel embedded flaws, Theor. Appl. Fract. Mech. 110 (2020), 103448.

[27] M. Bahaaddini, P.C. Hagan, R. Mitra, M.H. Khosravi, Experimental and numerical study of asperity degradation in the direct shear test, Eng. Geol. 204 (2016) 41–52.

[28] V. Sarfarazi, A. Ghazvinian, W. Schubert, M. Blumel, H.R. Nejati, Numerical Simulation of the Process of Fracture of Echelon Rock Joints, Rock Mech. Rock Eng. 47 (4) (2014) 1355–1371.

[29] M. Jiang, T. Jiang, G.B. Crosta, Z. Shi, H.e. Chen, N. Zhang, Modeling failure of jointed rock slope with two main joint sets using a novel DEM bond contact model, Eng. Geol. 193 (2015) 79–96.

[30] X. Luo, P. Cao, Q. Lin, S.u. Li, Mechanical behaviour of fracture-filled rock-like specimens under compression-shear loads: An experimental and numerical study, Theor. Appl. Fract. Mech. 113 (2021) 102935, https://doi.org/10.1016/j.tafmec.2021.102935.

[31] M. Nitka, A. Grabowski, Shear band evolution phenomena in direct shear test modelled with DEM, Powder Technol. 391 (2021) 369–384.

[32] M. Saadat, A. Taheri, Y. Kawamura, Incorporating asperity strength into rock joint constitutive model for approximating asperity damage: An insight from DEM modelling, Eng. Fract. Mech. 248 (2021) 107744, https://doi.org/10.1016/j.engfracmech.2021.107744.

[33] A.A. Owayo, F.C. Teng, W.C. Chen, DEM simulation of crack evolution in cement-based materials under inclined shear test, Constr. Build. Mater. 301 (2021), 124087.

[34] M. Jiang, J. Liu, G.B. Crosta, T. Li, DEM analysis of the effect of joint geometry on the shear behavior of rocks, Comptes Rendus Mécanique. 345 (11) (2017) 779–796.

[35] R.-H. Cao, R. Yao, T. Hu, C. Wang, K. Li, J. Meng, Failure and mechanical behavior of transversely isotropic rock under compression-shear tests: Laboratory testing and numerical simulation, Eng. Fract. Mech. 241 (2021) 107389, https://doi.org/10.1016/j.engfracmech.2020.107389.

[36] X. Tan, Y.-K. Ren, T.-L. Li, S.-H. Zhou, J.-C. Zhang, S.-K. Zhou, In-situ direct shear test and numerical simulation of slate structural planes with thick muddy interlayer along bedding slope, Int. J. Rock Mech. Min. Sci. 143 (2021), 104791.

[37] S.M. Seyyedan, A.A. Mirghasemi, S. Mohammadi, Numerical simulation of direct shear test on granular materials composed of breakable angular particles: A DEM-XFEM approach, Powder Technol. 391 (2021) 450–466.

[38] J.F. Hazzard, R.P. Young, Moment tensors and micromechanical models, Tectonophysics 356 (1-3) (2002) 181–197.

[39] Z. Chong, X. Li, P. Hou, X. Chen, Y. Wu, Moment tensor analysis of transversely isotropic shale based on the discrete element method, Int. J. Min. Sci. Technol. 27 (3) (2017) 507–515.

[40] Z. Chong, Q. Yao, X. Li, J. Liu, Investigations of seismicity induced by hydraulic fracturing in naturally fractured reservoirs based on moment tensors, J. Nat. Gas Sci. Eng. 81 (2020), 103448.

[41] J. Ma, S. Wu, X.-P. Zhang, Y. Gan, Modeling acoustic emission in the Brazilian test using moment tensor inversion, Comput. Geotech. 123 (2020), 103567.

[42] Q. Zhang, X.-P. Zhang, H. Zhang, P.-Q. Ji, S. Wu, J. Peng, Study of interaction mechanisms between hydraulic fracture and weak plane with different strengths and widths using the bonded-particle model based on moment tensors, Eng. Fract. Mech. 225 (2020), 106813.

[43] Q. Zhang, X.-P. Zhang, The crack nature analysis of primary and secondary cracks: A numerical study based on moment tensors, Eng. Fract. Mech. 210 (2019) 70–83.

[44] Y. Zhao, G. Zhao, J. Zhou, J. Ma, X. Cai, Failure mechanism analysis of rock in particle discrete element method simulation based on moment tensors, Comput. Geotech. 136 (2021), 104215.

[45] P. Martínez-Garzón, G. Kwiatek, M. Bohnhoff, G. Dresen, Volumetric components in the earthquake source related to fluid injection and stress state, Geophys. Res. Lett. 44 (2) (2017) 800–809.

[46] B.K. Atkinson, P.G. Meredith, Experimental fracture mechanics data for rocks and minerals, Fract. Mech. Rock. 8 (1987) 477–522.

[47] S. Wu, J. Ma, Y. Cheng, M. Xu, X. Huang, Numerical analysis of the flattened Brazilian test: Failure process, recommended geometric parameters and loading conditions, Eng. Fract. Mech. 204 (2018) 288–305.

[48] X. Zhou, Y. Xie, G. Long, J. Li, Effect of surface characteristics of aggregates on the compressive damage of high-strength concrete based on 3D discrete element method, Constr. Build. Mater. 301 (2021), 124101.

[49] Y. Li, W. Cai, X. Li, W. Zhu, Q. Zhang, S. Wang, Experimental and DEM Analysis on Secondary Crack Types of Rock-Like Material Containing Multiple Flaws Under Uniaxial Compression, Appl. Sci. 9 (2019) 1749.

[50] Y. Li, W. Cai, W. Zhu, Z. Dong, Q. Zhang, Particle flow analysis of parallel double crack evolution under uniaxial compression, J. Cent. South. Univ. 50 (2019) 3035–3045.

[51] X.-P. Zhou, J.-Z. Zhang, AE event rate characteristics of flawed granite: from damage stress to ultimate failure, Geophys. J. Int. 222 (2020) 795–814.

[52] X.-P. Zhou, J.-Z. Zhang, S.-Q. Yang, F. Berto, Compression-induced crack initiation and growth in flawed rocks: A review, Fatigue Fract. Eng. Mater. Struct. 44 (7) (2021) 1681–1707.

[53] X.-P. Zhou, J.-Z. Zhang, Damage progression and acoustic emission in brittle failure of granite and sandstone, Int. J. Rock Mech. Min. Sci. 143 (2021) 104789, https://doi.org/10.1016/j.ijrmms.2021.104789.

[54] A. Lisjak, Q. Liu, Q. Zhao, O.K. Mahabadi, G. Grasselli, Numerical simulation of acoustic emission in brittle rocks by two-dimensional finite-discrete element analysis, Geophys. J. Int. 195 (2013) 423-443.

[55] W. Sun, S. Wu, X. Xu, Mechanical behaviour of Lac du Bonnet granite after high-temperature treatment using bonded-particle model and moment tensor, Comput. Geotech. 135 (2021) 104132, https://doi.org/10.1016/j.compgeo.2021.104132.

[56] Q. Zhang, X.-P. Zhang, S.-Q. Yang, A numerical study of acoustic emission characteristics of sandstone specimen containing a hole-like flaw under uniaxial compression, Eng. Fract. Mech. 242 (2021), 107430.

[57] K. Duan, C.Y. Kwok, Q. Zhang, J. Shang, On the initiation, propagation and reorientation of simultaneously-induced multiple hydraulic fractures, Comput. Geotech. 117 (2020), 103226.

[58] Y. Zhao, L. Zhang, W. Wang, C. Pu, W. Wan, J. Tang, Cracking and Stress-Strain Behavior of Rock-Like Material Containing Two Flaws Under Uniaxial Compression, Rock Mech. Rock Eng. 49 (7) (2016) 2665–2687.

[59] S.-Q. Yang, Y.-H. Huang, H.-W. Jing, X.-R. Liu, Discrete element modeling on fracture coalescence behavior of red sandstone containing two unparallel fissures under uniaxial compression, Eng. Geol. 178 (2014) 28–48.

[60] A. Tordesillas, S. Pucilowski, Q. Lin, J.F. Peters, R.P. Behringer, Granular vortices: Identification, characterization and conditions for the localization of deformation, J. Mech. Phys. Solids. 90 (2016) 215–241.
[61] K.e. Zhang, Y. Chen, W. Fan, X. Liu, H. Luan, J. Xie, Influence of Intermittent Artificial Crack Density on Shear Fracturing and Fractal Behavior of Rock Bridges: Experimental and Numerical Studies, Rock Mech. Rock Eng. 53 (2) (2020) 553–568.
[62] C. Yu, V. Vavryčuk, P. Adamová, M. Bohnhoff, Moment Tensors of Induced Microearthquakes in The Geysers Geothermal Reservoir From Broadband Seismic Recordings: Implications for Faulting Regime, Stress Tensor, and Fluid Pressure, J. Geophys. Res. Solid Earth. 123 (2018) 8748–8766.
[63] D. Li, E. Wang, X. Kong, M. Ali, D. Wang, Mechanical behaviors and acoustic emission fractal characteristics of coal specimens with a pre-existing flaw of various inclinations under uniaxial compression, Int. J. Rock Mech. Min. Sci. 116 (2019) 38–51.
[64] W. Pan, X. Wang, Q. Liu, Y. Yuan, B. Zuo, Non-parallel double-crack propagation in rock-like materials under uniaxial compression, Int. J. Coal Sci. Technol. 6 (3) (2019) 372–387.
[65] Q. Lin, P. Cao, G. Wen, J. Meng, R. Cao, Z. Zhao, Crack coalescence in rock-like specimens with two dissimilar layers and pre-existing double parallel joints under uniaxial compression, Int. J. Rock Mech. Min. Sci. 139 (2021), 104621.
[66] V. Vavryčuk, Moment tensor decompositions revisited, J. Seismolog. 19 (1) (2015) 231–252.